Color-changeable properties of plasmonic waveguides based on Se-doped CdS nanoribbons

Zheyu Fang,[1] Shan Huang,[1] Yanwei Lu,[1] Anlian Pan,[2] Feng Lin,[1] and Xing Zhu[1,3,*]
[1]*School of Physics, State Key Laboratory for Mesoscopic Physics, Peking University, Beijing 100871, China*
[2]*Micro-Nano Technologies Research Center, Hunan University, Changsha 410082, China*
[3]*National Center for Nanoscience and Technology, Beijing 100190, China*
(Received 15 March 2010; revised manuscript received 6 July 2010; published 3 August 2010)

The color-changeable optical property induced by the resonance of surface-plasmon polaritons (SPPs) based on a ternary alloy $CdS_{0.65}Se_{0.35}$ (CdSSe) nanoribbon partly placed on an Ag film was reported. The spectroscopic redshift of *in situ* CdSSe photoluminescence under different incident laser powers was characterized by using scanning near-field optical microscopy. The propagation length, mode area, and confinement factor of the SPPs were also investigated. The trade-off between the spectroscopic shift and plasmonic resonance was demonstrated with the Franz-Keldysh effect and simulated by using the finite-difference time-domain method. The suggested plasmonic structure provides valuable information for the implementation of photonic integrated nanocircuits, especially for the color-changeable plasmonic device.

DOI: 10.1103/PhysRevB.82.085403 PACS number(s): 68.37.Uv, 73.20.Mf, 42.82.Et, 78.55.Cr

I. INTRODUCTION

Surface-plasmon polaritons (SPPs) are electromagnetic surface modes confined at a metal-dielectric interface due to the resonant interaction between the electromagnetic wave and surface electrons of the metal.[1] A variety of SPP waveguide structures, such as plasmonic metal strips,[2] grooves milling in the metal surface,[3] as well as metamaterial heterostructures[4] have been investigated with the advantage of nanofabrication techniques. However, because of Ohmic losses, the SPP wave experiences huge attenuation and its propagation length is limited to the order of 10 μm in the case of noble metals at visible wavelengths. Thus most of recent investigations related to the SPP excitation and propagation were focused in the range of telecommunication wavelength in order to gain a longer propagation length.[3–6]

The dielectric-metal interface is known as to support the SPP propagation characterized with a propagation constant β determined by corresponding metal and dielectric constants, ε_m and ε_d, and the incident light wavelength λ. The real part of β is related to the SPP effective refractive index, implying that the presence of a dielectric layer on the metal surface results in a higher SPP index as compared to the air-metal interface.[1] SiO_2 ridges on the Au surface were used to generate dielectric-loaded SPPs (DLSPPs) that achieved smaller bend losses and were used as basic building blocks and interconnects in integrated circuits.[7,8] A DLSPP waveguide provides an effective way to realize the SPP propagation in the subwavelength scale. However, the SiO_2-based DLSPP is limited at the controlling or modulating of the SPP emission for an optical nanocircuit, and this is essential for the integrated plasmonic device in the future.

On the other side, one-dimensional semiconductors are attractive for their functions as the optical waveguide for integrated circuits and basic elements of the photonic device.[9] Due to the optical confinement at radial directions, nanoribbons are found to have potential optical transport applications. CdS nanoribbons present a variety of chemical and optical specificities, sensibilities, and especially doping characters that are crucial for the development of active and dynamic functionalities addressed either optically or electrically, such as modulators or switches. Different Se composition dopings regulated optical transport properties of the CdS nanoribbon and gave rise to a significant photoluminescence (PL) shift for the fluorescence guided wave, and this has been explained by the semiconductor self-absorption effect,[10] i.e., the Urbarch tail, an extension of the density of state into the band gap near main edges of bands, and induce an exponential tail near the fundamental absorption edge at the long-wavelength direction. However, this color-changeable transport property can only be modulated by the waveguide distance, i.e., there is a trade-off between the spectroscopic shift and the dissipation of the emission intensity.

In previous works, the excitation and propagation of CdS-based DLSPP modes were characterized by using scanning near-field optical microscopy (SNOM);[11,12] the coupling of a focused SPP wave into a CdS-based DLSPP waveguide, and even the CdS-based DLSPP laser were reported recently.[13,14] In this work, a single ternary alloy $CdS_{0.65}Se_{0.35}$ (CdSSe) nanoribbon was partly placed on a Ag film and used as the DLSPP waveguide. It allows us to investigate the DLSPP mode propagation length, mode area, and confinement factor in a single configuration. It also combines both merits of the semiconductor PL modulation (with the Se doping) and the SPP-induced electric field enhancement. The spectroscopic shift of the *in situ* SPP emission was found strongly related to the power of the incident laser. It indicates the possibility of a visible region color-tunable device in the future.

II. METHODS AND EXPERIMENTS

Figure 1(a) is the scanning electron microscope (SEM) and transmission electron microscope (TEM) (inset) images for CdSSe nanoribbons that possess fairly uniform rectangular cross sections with a dimension around 600 nm $\times$300 nm. The Ag film with a 15 nm thickness and a 2 nm roughness was fabricated by using the electron-beam lithography technique on a smooth sapphire surface. The nanoribbon was deposited onto the Ag film by using the polymethylmethacrylate-(PMMA) mediated nanotransfer printing

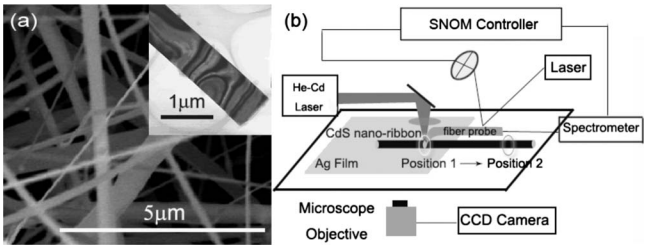

FIG. 1. (a) SEM and TEM (inset) images for the CdSSe nanoribbon. (b) Schematic of the experimental setup and process.

technique.[15] Under the incident laser of 442 nm, *in situ* spatial resolved PL spectra of the CdSSe nanoribbon with one end placed on the Ag film were recorded by using the SNOM.

The experimental schematic is shown in Fig. 1(b). The incident laser with a focus diameter of 1 μm evenly illuminated the CdSSe nanoribbon. Positions 1 and 2 indicate the area of the nanoribbon placed on the Ag film and on the sapphire surface, respectively. A SNOM probe with a 100 nm apex tip was used to collect *in situ* near-field spectra of positions 1 and 2 under different laser powers from 12 to 92 mW. Near-field PL spectra at these two positions were effectively investigated and compared by using this technique.

A. SPP guiding in the DLSPP structure

The direction of SPP propagation is considered along the z axis (Fig. 2) and the electric field can be derived as

$$\boldsymbol{E} = \boldsymbol{E}_p(y)\exp[i(\omega t - \beta z)], \tag{1}$$

where $\boldsymbol{E}_p$ denotes the component of the electric field, such as the case of TM modes in the (y,z) plane. β is the complex propagation constant $\beta=\beta'-i\beta''$ that is related to the mode effective index according to $\beta'=k_0N_{eff}^*=(2\pi/\lambda)N_{eff}^*$ and propagation length as $L^*=1/(2\beta'')$. It is instructive to consider the SPP dispersion relation of a metal-dielectric interface, and can be thought of as a limiting thickness h being either small ($\ll\lambda/2$) or large ($\approx\lambda/2$), λ is the wavelength of the incident laser. The corresponding SPP dispersion relation is given by[1]

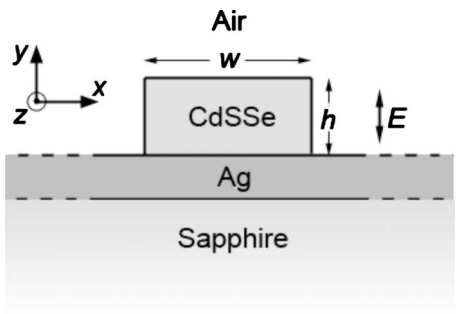

FIG. 2. Cross-sectional view of the CdSSe nanoribbon based DLSPP waveguide under investigation.

$$\beta = k_0\sqrt{\frac{\varepsilon_m\varepsilon_d}{\varepsilon_m+\varepsilon_d}}, \tag{2}$$

where ε_m and ε_d are complex permittivities of the metal and dielectric, respectively. It is expected that, for a thin dielectric film layer, the fundamental mode becomes progressively close to a SPP propagating along the Ag-air interface; correspondingly, for a thick film layer, the result should approach those of a SPP at the Ag-CdSSe interface. Between these extremes, it is expected that the SPP mode effective index of the DLSPP structure is monotonously decreasing with the dielectric thickness owing to an increasing part of the SPP field penetrates in the air above the CdSSe nanoribbon.

On the other side, the excitation of SPP guided mode is governed by a phase matching condition,

$$k_0N_1\sin\theta\cdot\sin\delta = k_0N_{eff}^*, \tag{3}$$

where k_0 is the free-space wave vector, N_1 is the refractive index of the dielectric, and N_{eff} is the associated complex effective index. The real part of N_{eff}^* is used in Eq. (3) due to the reason that the Ag layer is a source of Ohmic and radiative losses. Most of the incident laser penetrates the CdSSe nanoribbon (300 nm thickness), thus a continuum wave vectors are generated by the scattering light on the Ag film. The phase-matching condition given by Eq. (3) is fulfilled by some of wave vectors and the SPP resonance is occurred at the interface between the nanoribbon and the Ag film. Localized SPs (LSPs) are also excited by the incident laser on the Ag surface (2 nm roughness). When LSPs interacted with the rough surface of the Ag film, they can couple to SPPs spontaneously.[1]

B. CdSSe nanoribbons

The CdSSe nanoribbon was synthesized based on a physical evaporation in the presence of a Au catalyst.[16] Before growth, equimolar commercial-grade CdS and CdSe powders were placed onto a ceramic plate at the center of a quartz tube and was inserted into a horizontal tube furnace. Several pieces of silicon slices coated with ~10 nm Au film were placed downstream of the gas flow for deposition of specimens. Prior to heating, a high-purity He gas was introduced into the quartz tube with a constant flow rate (5 SCCM) to purge the O_2 inside. After a period of time, the furnace was rapidly heated to 800 °C and maintained at this temperature for ~2 h. Spongelike products were deposited on surfaces of silicon wafers.

The SEM image of CdSSe nanoribbons was recorded using a scanning electron microscopy (SEM, Hitachi S-5200). Morphology and high-resolution images were observed with a transmission electron microscope (TEM, Philip Tecnai 20). PL spectra of CdSSe specimens were taken at the room temperature using the 442 nm line of a He-Cd laser as the excitation source.

C. Scanning near-field optical microscopy

The SNOM consists of a scanner NSOM-100 (Nanonics Co.), an electronic controller SPM-100 (RHK Co.), and a

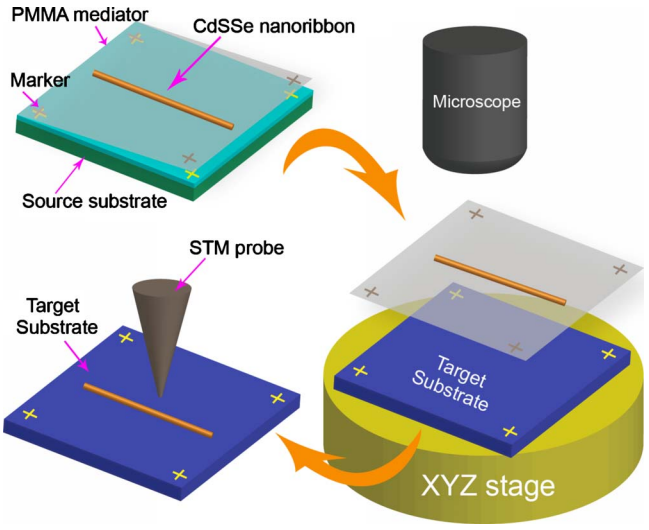

FIG. 3. (Color online) The procedure of the PMMA-mediated nanotransfer printing technique (Ref. 15).

spectroscopy iHR-550 (Jobin Yvon Co.).[17–19] The scanner is situated on the sample stage of an inverted optical microscope (Olympus IX70). The Al-coated near-field optical tip used in this experiment is the cantilever-shaped and tapered optical fiber with a 100 nm apex diameter (Nanonics Co.). A focused He-Cd laser (442 nm) evenly illuminated the nanoribbon deposited on a Ag film (15 nm thickness) and the SNOM tip with the lateral resolution of about 50 nm was used to collect PL spectra. A chromatic color charge-coupled-device (CCD) through an objective lens was used to record the far-field and optical transmission images.

D. PMMA-mediated nanotransfer printing

The PMMA-mediated nanotransfer printing technique aims at creating arbitrary purpose-directed nanostructures with various nanoscale building blocks by using PMMA film as a macroscopic mediator for handling tiny nanoscale building blocks.[15] The transfer process involves four basic steps as shown in Fig. 3, including loading nanomaterials onto a PMMA mediator, peeling off the mediator from the source substrate, attaching the mediator to the target substrate, and releasing the loaded nanomaterial to the target substrate.

To load nanomaterials on to the mediator, a PMMA solution was spin coated onto the source substrate and then baked to obtain a thin-film embedding nanomaterials. The peeling-off of the PMMA film is the key step of this transfer approach. To make the peeled-off film adhere firmly to the target substrate, the film was annealed at 50 °C for 5 min after being attached onto the target substrate with an aligning system (XYZ stage). Markers were made at four corners for the alignment. To release nanomaterials to the target substrate, the PMMA film was dissolved in an acetone vapor, a commonly used solvent for removing the PMMA film in the lift-off process without perturbing underlying nanomaterials. The alignment could be precisely to the nanometer scale if the scanning tunneling microscopy probe was also used to drive and redirect the nanomaterial within the scale of 100 nm in plane.

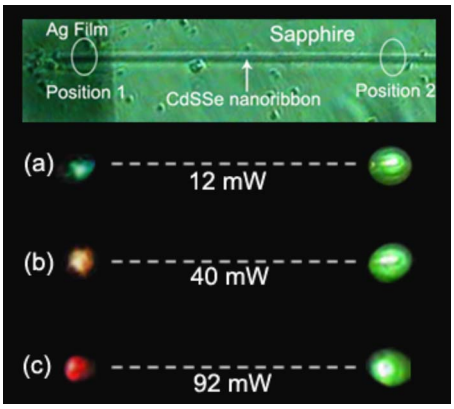

FIG. 4. (Color online) The optical transmission image for the CdSSe nanoribbon partly placing on the Ag film. [(a)–(c)] The sequence of dark-field PL spots corresponding to positions 1 and 2, under 12 mW, 40 mW, and 92 mW laser illumination, respectively. Dashed lines indicate the location of the CdSSe nanoribbon.

III. RESULTS AND DISCUSSIONS

The *in situ* PL of a CdSSe nanoribbon was recorded with a color CCD camera. On the top of Fig. 4 is an optical transmission image for a CdSSe nanoribbon with one end placed on a Ag film. (a)–(c) are the sequence of color-changeable PL spots excited under different powers of the incident laser (442 nm). PL spots at left and right sides are related to the recording area of positions 1 and 2 that are indicated in the optical transmission image, respectively. PL spots are connected by dashed lines that indicate the location of the nanoribbon. For the position 1, the color of PL spots was changed from green to orange and yellow-red with the incident laser power increased from 12 to 40 mW, and 92 mW. At the meantime, PL spots from position 2 have no obvious change under these different laser powers.

The excitation of SPP couples most of the incident laser energy into SPP modes, confined at the interface between the Ag film and the CdSSe nanoribbon, and induces dissipation for the intensity of the *in situ* PL emission. Spectroscopic results, detected by the SNOM, are shown in Fig. 5(a) as near-field PL spectra for positions 1 and 2, respectively. Here, positions 1 and 2 are the same areas indicated in Fig. 1(b) and also in the optical transmission image of Fig. 4.

For position 1, the PL spectra series describes a trade-off between the incident laser power and the *in situ* emission wavelength changing. Apparently, emission bands exhibit a significant spectroscopic redshift with the increasing of the excitation laser power. However, PL spectra from position 2 experience nearly no energy shift but only the decrease in the emission intensity. This spectroscopic shift with respect to the incident laser power is plotted in Fig. 5(b) for positions 1 and 2, respectively. Similar experiments of an undoped CdS nanoribbon are also investigated and the result is plotted for the comparison with the Se-doped one in Fig. 5(b). Both Se-doped and undoped CdS nanoribbons exhibit same spectroscopic shift phenomena for the area of position 1 (the area of nanoribbon on the Ag film). It also can be seen that the case of the Se-doped CdS nanoribbon exhibits a higher maximum saturation value than the undoped one, e.g., the Se-

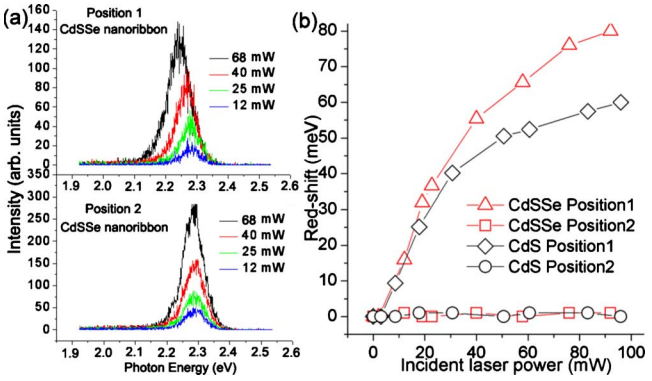

FIG. 5. (Color online) (a) *In situ* near-field PL spectra of CdSSe nanoribbon for both positions 1 and 2 under various incident laser powers. (b) The plot of redshift value with respect to the excitation laser for both CdSSe and CdS nanoribbons at positions 1 and 2, respectively.

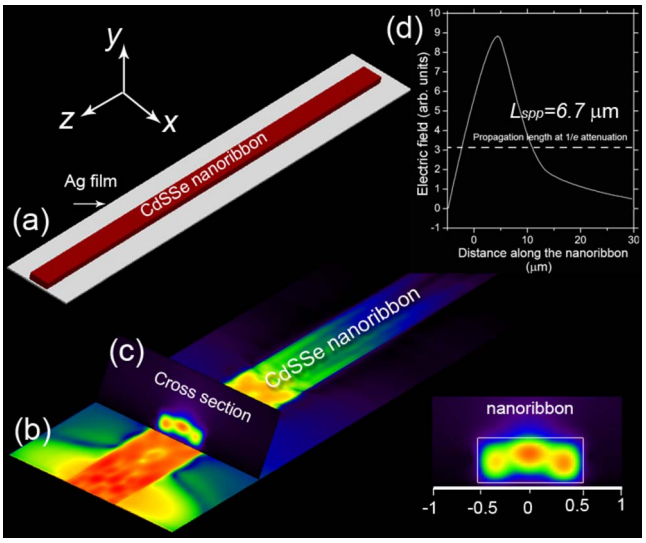

FIG. 6. (Color online) (a) The simulation model for a CdSSe nanoribbon deposited on a Ag film. (b) Steady-state image of the simulated electric field at the interface between the Ag film and the nanoribbon. (c) A cross section of the electric field distribution of the CdSSe nanoribbon inside region. (d) Intensity distribution along the nanoribbon center.

doped nanoribbon has a maximum redshift of ~80 meV, whereas the value for an undoped one is ~60 meV. For each incident laser power, the redshift value of Se-doped nanoribbon is larger than the undoped one, e.g., 65–50 meV, when the laser power is fixed at 68 mW.

For position 2 (the area of nanoribbon on the sapphire), there is nearly no spectroscopic shift for recorded PL spectra under any incident laser powers. These PL spectra indicate a good agreement with the color-changeable observation of dark-field PL spots, as shown in Figs. 4(a)–4(c). The discrepancy for Se-doped and undoped CdS nanoribbons comes from the distinctive composition-related local structural disorder.[10] With the Se doping, a CdS nanoribbon can have a broader absorption edge, indicates an increase in the structural disorder degree induced by the composition fluctuation, and finally to have a more-noticeable spectra spectroscopic redshift with the increasing of the incident laser power.

A. FDTD simulations

Finite-difference time-domain (FDTD) simulations using an eigenmode solver at the front edge boundary were preformed to confirm the field enhancement induced by the SPP resonance. The method of FDTD is particularly suited in the investigation of waveguide because it calculates electric fields inside and outside the architecture and provides a complex effective index for the guided mode. Figure 6(a) is the model of a CdSSe nanoribbon (refractive index n=2.64) placed on a Ag film (15 nm thickness, permittivity= $-7.6321+0.7306i$). Parameters of the considered waveguide are h=300 nm, w=600 nm, as denoted in Fig. 2. The CdSSe waveguide is illuminated by a Gaussian beam of 442 nm.

The steady-state image of the simulated electric field at the interface between the nanoribbon and the Ag film, and a cross section of the electric field distribution of the CdSSe nanoribbon inside region, are illustrated in Figs. 6(b) and 6(c), respectively. The simulation shows that the electric field is well confined by the dielectric structure and has its maximum at the Ag-CdSSe interface as expected from a SPP wave, and it can be estimated as ~10 mV/nm for this plasmonic structure by using the commercial software XFDTD (Remcom Inc.). Figure 6(d) is the SPP modes evolution along the propagation direction. The decay along the propagation is exponential. We deduce from Fig. 6(d) a propagation length at $1/e$ attenuation of L_{SPP}=6.7 μm.

B. Mode area and confinement factor

To evaluate the performance of a waveguide we introduce a set of parameters, the confinement factor R, and the mode area A_e (Ref. 20). Berini[20,21] proposed the concept of figures of merit for determining optimized dimensions of SPP waveguides. For SPP waveguides consisting of metal strips, small sizes and limited losses are prerequisites. The figure of merit for these parameters was defined as

$$M_1^{2D} = \sqrt{\frac{\pi}{A_e}(2 \times L_{\mathrm{SPP}})}. \tag{4}$$

This figure of merit adapted for both propagation length and mode area, however, it lacks the information on the SPP modes confinement that is of great importance for applications in active plasmonics. For the structure of DLSPP waveguide, the amount of SPP modes sustained inside the CdSSe nanoribbon determines how strong the influence of changes is in the whole mode. The confinement factor measures the proportion of the mode energy inside the waveguide. A higher degree of confinement would ensure a stronger interaction between SPPs and an active material. The confinement factor R can be calculated as[22]

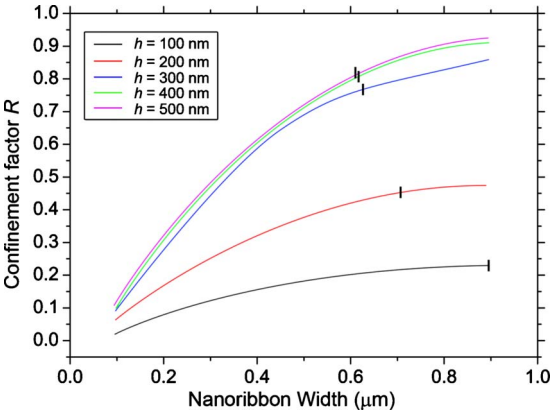

FIG. 7. (Color online) Confinement factor calculated by using EIM method for several CdSSe nanoribbon thicknesses as a function of nanoribbon width. Vertical crosses indicate the cutoff width.

$$R = \frac{\int\int_{guide} \boldsymbol{P} \cdot d\boldsymbol{S}}{\int_{-\infty}^{+\infty}\int_{z>0} \boldsymbol{P} \cdot d\boldsymbol{S}}, \tag{5}$$

where $\boldsymbol{P}$ is the Poynting vector. Consequently, we limit the integration above the substrate for the normalization.

Using the effective index model (EIM), as described in detail in Ref. 23, we determine the confinement of the SPP mode supported by this CdSSe-based DLSPP waveguide by using Eq. (5). The mode confinement as a function of the nanoribbon width w and for different CdSSe thicknesses h, are presented in Fig. 7. The cutoff cross indicates most of SPP modes concentrated in the nanoribbon subregion so that the field magnitude in the four corner regions are small enough to be neglected. Second, the field confinement increases with CdSSe thickness and tends to saturate for the thickness over than 400 nm. Third, increasing the width of the CdSSe allows the excitation of dipole, quadrupole, and higher-order modes in the waveguide and localized at Ag nanoislands (2 nm roughness for the Ag film surface).[23] In the meantime, a Coulomb force of electron oscillations is collected at opposite sides of the Ag nanoisland and causes a huge electric field intensity than the excitation background.[24]

C. Franz-Keldysh effect

The Franz-Keldysh effect is a physical phenomenon associated to the influence of a high electric field on the near band-edge absorption, and indicates the electric field may cause a redshift of the absorption edge, giving rise to the presence of an absorption "tail" for band-to-band transitions.[25] According to the Franz-Keldysh effect, free-electron wave functions modify into Airy functions rather than plane waves, and exponentially decreases in the band-gap region when a semiconductor is under a high electric field. The Airy function includes a "tail" and extends into the classically forbidden band gap. According to Fermi's golden rule, the more overlap there is between wave functions of a free electron and a hole, the stronger the optical absorption will be. The Airy tails slightly overlap even if the electron and hole are at slightly different potentials (slightly different physical locations along the field). As a result, a subband-gap optical absorption occurs, interpreted as a photon-assisted tunneling through the forbidden band region, with the photon energy smaller than the energy gap (E_{gap}),[26] as schematically shown in Fig. 8.

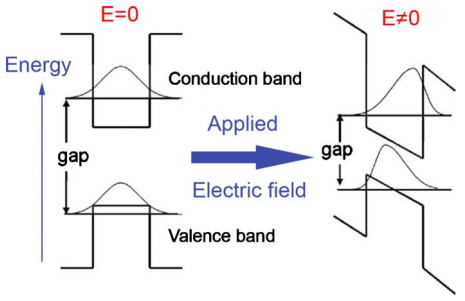

FIG. 8. (Color online) The band structure of a quantum well without and with an applied static electric field. With external electric field, the quadrate well (barrier) potential turns to be triangular well (barrier) potential, and results in a narrowed gap.

In the subband region, the Franz-Keldysh absorption coefficient α versus $(h\nu)$ can be approximated by an exponential function,

$$\alpha(h\nu) \sim \exp\left(-\left|\frac{h\nu - E_{gap}}{\Delta E}\right|^{3/2}\right) \tag{6}$$

with ΔE given by

$$\Delta E = \frac{2}{3}\frac{(e\hbar\xi)^{2/3}}{(m^*)^{1/3}}, \tag{7}$$

where ξ, m^*, e, and $\hbar$ are the electric field, effective mass, electron charge, and Planck's constant. On the other side, emission spectra $S(\beta)$ for this hybrid plasmonic structure under various incident laser powers (β) can be defined by

$$S(\beta) = S_0 e^{-\alpha(h\nu)\beta}, \tag{8}$$

where S_0 is the saturated spectrum correlated with the maximum excitation power.

Curves in Fig. 9(a) are spectra of the CdSSe nanoribbon placed on the Ag film calculated by using above equations. The power of incident laser is changed from 12 to 68 mW. Similar to the experimental result, calculated spectra exhibit a significant spectroscopic redshift with the increasing of the incident power, i.e., the value of β in Eq. (8). Two red dashed lines in Fig. 9(b) are theoretical results for the redshift value with respect to incident powers for Se-doped and undoped CdS nanoribbons, respectively. The $h\nu$ for a CdSSe one-dimensional nanostructure at room temperature is ~36 meV and the value of the energy gap E_{gap} is taken from the corresponding bulk single crystal.[27] In Fig. 9(b), black solid triangles and rhombuses are experimental values of Se-doped and undoped CdS nanoribbons, respectively. Apparently, theoretical calculated values have similar spectroscopic characteristics in comparison with experimental results, i.e., the redshift is saturated when the power of incident laser is larger than 100 mW and the CdSSe nanoribbon

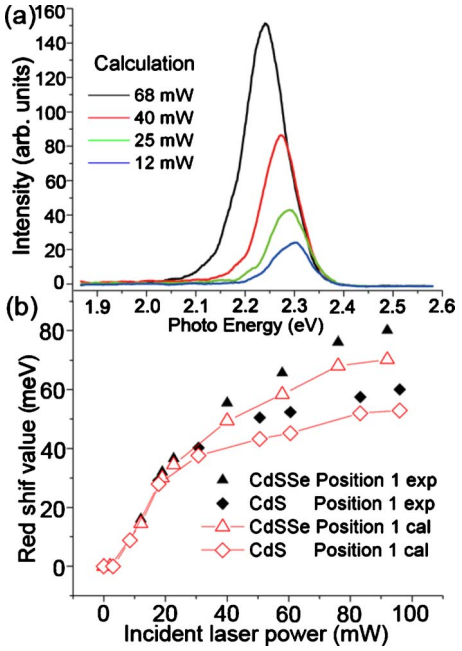

FIG. 9. (Color online) (a) Spectra of the CdSSe nanoribbon for calculations with the Franz-Keldysh effect. (b) Plots for the comparison between experiments and calculations of redshift values of Se-doped and undoped CdS nanoribbons under the condition of the nanoribbon placed on the Ag film (position 1).

has a larger redshift value than the undoped CdS under every incident laser power. The agreement between experimental and calculation results verifies the assumption that the spectroscopic shift is induced by the Franz-Keldysh effect when the nanoribbon is seized with the huge electric field induced by the resonance of DLSPPs at the interface between the Ag film and the CdSSe nanoribbon. It is noticed that theoretical calculations show a discrepancy with experimental results. Considering the small size in the radial direction, CdSSe nanoribbons contain more defects at the surface region than the bulk material. Thus, parameters of the bulk crystal used in calculations results a discrepancy to the theoretical and experimental redshift values.

IV. CONCLUSIONS

Color-changeable properties of the plasmonic waveguide based on the CdSSe nanoribbon are investigated by using SNOM under various incident laser powers. An enhanced electric field resulted by the DLSPP resonance is confined at the interface between the Ag film and the CdSSe nanoribbon. The spectroscopic redshift of the Se-doped CdS nanoribbon was configured as the color changing of PL spots from green to red and was compared with the result of the undoped CdS nanoribbon. DLSPP modes area and confinement factor are characterized with EIM method. The Franz-Keldysh effect associated to the influence of a high electric field on the near band-edge absorption is used to explain this spectroscopic redshift phenomenon. With FDTD simulations, the intensity of the electric field induced by the SPP resonance is estimated and utilized for theoretical spectroscopic calculations. Theoretical redshifts have a good agreement with experimental recordings. The suggested plasmonic structure has potential applications for the future photonics, and integrated circuits, especially for the color-changeable plasmonic device.

ACKNOWLEDGMENTS

The work is supported by the National Basic Research Program of China (973 Program) Grant No. 2007CB936800 and the National Science Foundation of China (Grant No. 10574002).

*Corresponding author; zhuxing@pku.edu.cn

[1] H. Raether, in *Surface Plasmons*, edited by G. Hohler (Springer, Berlin, 1988).
[2] L. Pyayt, B. Wiley, Y. N. Xia, A. Chen, and L. Dalton, Nat. Nanotechnol. **3**, 660 (2008).
[3] V. S. Volkov, S. I. Bozhevolnyi, S. G. Rodrigo, L. Martin-Moreno, F. J. Garcia-Vidal, E. Devaux, and T. W. Ebbesen, Nano Lett. **9**, 1278 (2009).
[4] X. Zhang and Z. W. Liu, Nature Mater. **7**, 435 (2008).
[5] E. Verhagen, L. Kuipers, and A. Polman, Nano Lett. **7**, 334 (2007).
[6] S. I. Bozhevolnyi, V. S. Volkov, E. Devaux, J.-Y. Laluet, and T. W. Ebbesen, Nature (London) **440**, 508 (2006).
[7] A. V. Krasavin and A. V. Zayats, Phys. Rev. B **78**, 045425 (2008).
[8] B. Steinberger, A. Hohenau, H. Ditlbacher, A. L. Stepanov, A. Drezet, F. R. Aussenegg, A. Leitner, and J. R. Krenn, Appl. Phys. Lett. **88**, 094104 (2006).
[9] J. T. Hu, T. W. Odom, and C. M. Lieber, Acc. Chem. Res. **32**, 435 (1999).
[10] A. L. Pan, X. Wang, P. B. He, Q. L. Zhang, Q. Wang, M. Zacharias, X. Zhu, and B. S. Zou, Nano Lett. **7**, 2970 (2007).
[11] Z. Y. Fang, X. J. Zhang, D. Liu, and X. Zhu, Appl. Phys. Lett. **93**, 073306 (2008).
[12] Z. Y. Fang, S. Huang, F. Lin, and X. Zhu, Opt. Express **17**, 20327 (2009).
[13] Z. Y. Fang, C. F. Lin, R. M. Ma, S. Huang, and X. Zhu, ACS Nano **4**, 75 (2010).
[14] R. F. Oulton, V. J. Sorger, T. Zentgraf, R. M. Ma, C. Gladden, L. Dai, G. Bartal, and X. Zhang, Nature (London) **461**, 629 (2009).
[15] L. Y. Jiao, B. Fan, X. J. Xian, Z. Y. Wu, J. Zhang, and Z. F. Liu, J. Am. Chem. Soc. **130**, 12612 (2008).
[16] A. L. Pan, H. Yang, R. C. Yu, and B. S. Zou, Nanotechnology **17**, 1083 (2006).
[17] Z. Y. Fang, F. Lin, S. Huang, W. T. Song, and X. Zhu, Appl. Phys. Lett. **94**, 063306 (2009).
[18] Z. Y. Fang, T. Dai, Q. Fu, B. Zhang, and X. Zhu, J. Microsc. **235**, 138 (2009).
[19] Z. Y. Fang, Y. W. Lu, L. R. Fan, C. F. Lin, and X. Zhu, Plasmonics **5**, 57 (2010).

[20] P. Berini, Opt. Express **14**, 13030 (2006).
[21] R. Buckley and P. Berini, Opt. Express **15**, 12174 (2007).
[22] J. Grandidier, S. Massenot, G. Colas des Francs, A. Bouhelier, J.-C. Weeber, L. Markey, A. Dereux, J. Renger, M. U. González, and R. Quidant, Phys. Rev. B **78**, 245419 (2008).
[23] T. Holmgaard and S. I. Bozhevolnyi, Phys. Rev. B **75**, 245405 (2007).
[24] R. F. Oulton, V. J. Sorger, D. A. Genov, D. F. P. Pile, and X. Zhang, Nat. Photonics **2**, 496 (2008).
[25] V. Perebeinos and P. Avouris, Nano Lett. **7**, 609 (2007).
[26] A. Cavallini, L. Polenta, and M. Rossi, Nano Lett. **7**, 2166 (2007).
[27] V. P. Kunets, N. R. Kulish, V. P. Kunets, and M. P. Lisitsa, Semicond. Phys., Quantum Electron. Optoelectron. **5**, 9 (2002).